An Enhanced Linear Active Disturbance Rejection Controller for High Performance PMBLDCM Drive Considering Iron Loss

Prashant Kumar, *Graduate Student Member, IEEE*, Abdul R. Beig, *Senior Member, IEEE*, Devara Vijaya Bhaskar, *Member, IEEE*, Khaled Al Jaafari, *Senior Member, IEEE*, Utkal Ranjan Muduli, *Member, IEEE*, and Ranjan Kumar Behera, *Senior Member, IEEE*

***Abstract*—The use of position sensors for the variable frequency drive (VFD) has been verified for years. However, more reliable VFDs with smart autonomous systems require side-by-side implementation of sensor and/or sensorless operation. Recently developed active disturbance rejection control (ADRC) provides robustness to VFD uncertainty and its fast response to reject disturbances. Considering the iron loss effect as the disturbance to the permanent magnet brushless dc motor (PMBLDCM) performances, a novel ADRC is proposed in this article. The ADRC current controller considering the iron loss effect is proposed along with an estimation of the back electromagnetic force disturbance used for the position/speed estimation. The proposed controller incorporates a structured inner and outer closed-loop ADRC that considers process delays and extended state observer dynamics. These dual ADRC-based control algorithms are verified for PMBLDCM drive both by simulation study and experimental findings. The improved performance of the proposed method is validated with a laboratory prototype of 2.5 kW PMBLDCM drive system.**

***Index Terms*—Active disturbance rejection control (ADRC), maximum torque per ampere (MTPA), permanent magnet brushless dc motor (PMBLDCM), sensorless operation, torque ripple minimization.**

I. Introduction

OWING to the improved torque-speed characteristics, higher torque to weight ratio, higher efficiency, better control sensitivity and low vibrations, the permanent magnet brushless dc motor (PMBLDCM) are preferred for low power electric vehicles and high precision industrial applications [1]. The normal operating conditions of PMBLDCM require six-step conduction mode control during which the inverter commutes in every 60 electrical degrees [2]. The commutation inaccuracies lead to torque ripple and poor efficiency [3], [4]. The torque ripple causes vibration, acoustic noise, and speed fluctuations, which restricts its use for high precision applications [5], [6]. In addition, torque ripple in PMBLDCM drive results in higher current ripples with increased copper losses and thus leads to decreased overall drive efficiency [7]. Enhancing motor torque performance with reduced torque ripple by minimizing copper loss is therefore a major concern in current research [8]–[10].

In literature, maximum torque per ampere (MTPA) control strategy has been investigated in order to reduce copper loss and enhance the drive efficiency [11], [12]. The direct (d) axis stator current component is considered as the torque controlling component resulting in cross-coupling effect, whereas quadrature (q) axis provides a flux controlling action. Hence, MTPA can be achieved either by nullifying the d-axis stator current component [12] or by developing the stator current with petal-wave pattern considering both dq-axis components [11]. MTPA strategy provided in [12] and [13] essentially includes q-axis current estimation in order to improve the PMBLDCM torque, thus reducing d-axis current to zero. In [14], MTPA is achieved by estimating the angle of the PMBLDCM model to increase the output torque with the predefined value of the stator current. In order to improve the precision of MTPA angle calculations, many offline and online parameter estimation models are proposed in [15] and [16]. However, the accurate estimation of MTPA angle during heavy load operation is not feasible as PMBLDCM electrical parameters differ considerably. Accurate modeling of PMBLDCM considering numerous aspects of design and material properties is more relevant to address torque ripple. Particularly, increase in temperature and magnetic saturation of permanent magnet leads to performance degradation. Iron loss, considering both hysteresis and eddy current losses, thereby leads to the performance degradation of PMBLDCM. In order to predict and evaluate the effect of iron loss, various iron loss based PMBLDCM models have been

Manuscript received October 12, 2020; revised February 12, 2021 and May 17, 2021; accepted June 6, 2021. Date of publication June 10, 2021; date of current version August 16, 2021. This work was supported in part by Abu Dhabi Education and Knowledge (ADEK) under Grant Abu Dhabi Award for Research Excellence AARE18-102 and in part by Khalifa University Advanced Power and Energy Center Award No. RC2-2018/21-06, Abu Dhabi, UAE. Recommended for publication by Associate Editor B. Mirafzal. *(Corresponding author: Prashant Kumar.)*

Prashant Kumar is with the Department of Electrical Engineering, IIT (ISM) Dhanbad, Dhanbad 826004, India, and also with the Khalifa University (KU), Abu Dhabi, UAE (e-mail: prashant.18dr0100@ee.iitism.ac.in).

Abdul R. Beig, Khaled Al Jaafari, and Utkal Ranjan Muduli are with the Advanced Power and Energy Center, Department of Electrical Engineering and Computer Science, Khalifa University (KU), Abu Dhabi, UAE (e-mail: balanthi.beig@ku.ac.ae; khaled.aljaafari@ku.ac.ae; utkal.pee17@iitp.ac.in).

Ranjan Kumar Behera is with the Department of Electrical Engineering, IIT Patna, Daulatpur 801103, India (e-mail: rkb@iitp.ac.in).

Devara Vijaya Bhaskar is with the Department of Electrical Engineering, IIT (ISM) Dhanbad, Dhanbad 826004, India (e-mail: devara@iitism.ac.in).

Color versions of one or more figures in this article are available at https://doi.org/10.1109/TPEL.2021.3088418.

Digital Object Identifier 10.1109/TPEL.2021.3088418

studied in the literature. In this article, a modified MTPA control strategy is provided, considering the effect of iron loss.

PMBLDCM with iron loss consideration is ubiquitous with instability and disruptions without proper control action. This often leads to inappropriate closed-loop control performance such as increment in torque ripple and deterioration in speed performance. The well-established indirect current control [11], direct torque control (DTC) [12], and model predictive control [17] do not deal with such disturbances. Over the past two decades, disturbance-based control techniques such as disturbance observer based control (DOBC) [18]–[22], extended state observer (ESO) [23]–[25], and active disturbance rejection control (ADRC) [19], [26]–[28] have been found to be a viable solution to the control problem described above. DOBC is mainly suitable for speed estimation where disturbances and uncertainties have to be canceled by an inverse plant model; however, the interface of low-pass filters (LPFs) remains challenging [21]. ADRC has proven to be efficacious in a number of industrial and academic researches by mitigating the challenges of LPF delay in case of DOBC [26], [28]. However, such enhanced control capabilities are not being investigated for PMBLDCM drive, where precision torque control with speed robustness is far more important. The basic structure of ADRC includes transient profile generator, tracking differentiator, and ESO whose task is to estimate uncertainties, unmodeled dynamics, and external disturbances [27]. The linear ESO (LESO) has advantages over nonlinear ESO considering the control complexities. LESO-based state feedback control is used to compensate the total disturbance at minimum tracking error which relaxes the necessity of accurate modeling of the system dynamic. A phase-locking loop observer (PLLO) based ADRC also improves the disturbance rejection property without increasing the algorithm complexity. An ADRC scheme is therefore proposed in this article, considering the impact of iron loss as a disturbance to the original model. Usually sensor-based mechanical rotor position estimation methods using an external high-resolution encoder or an internal hall-effect sensor are utilized for years in industrial applications. However, due to increased costs and mechanical maintenance, current research focuses more on the application of side-by-side sensor and/or sensorless rotor position/speed estimation methods. Recent sensorless methods documented in literature estimate the speed based on back electromagnetic force (EMF) method, a third harmonic method, a phase-locked loop (PLL) method, and flux linkage method [4], [8], [29]. However, this article analyzes the current ADRC-based disturbance estimation method corresponding to back EMF using ESO and further normalizes to determine the rotor position/speed of PMBLDCM, which enables sensorless operation. The estimated speed is provided as feedback to speed ADRC in order to achieve adequate tracking considering disturbances due to load torque variation and iron loss effect.

In this article, a current ADRC is introduced to provide optimized modulation control of three-phase three-level (TPTL) neutral point clamped (NPC) voltage source inverter (VSI). The TPTL-NPC VSI has a number of practical benefits, such as greater flexibility in the determination of switching vectors, lower voltage stress on semiconductor switches, reduced dv/dt, improved total harmonic distortion (THD), and lower torque ripple [30]. The main contributions of this article are as follows.

1) A PMBLDCM modeling, considering the effect of iron loss as a disturbance, is established by investigating the MTPA control as detailed in Section II.
2) An ADRC-based speed controller is proposed by observing the disturbances that correspond to load torque and iron losses for PMBLDCM drive. In addition, the speed is estimated through normalized back EMF disturbance to achieve sensorless operation and given in Section III.
3) A novel ADRC-based inner loop current control is proposed to minimize the current and torque ripple by estimating the disturbance correspond to back EMF of PMBLDCM.
4) The proposed speed ADRC and current ADRC with LESO and PLLO design are verified through simulation as well as experimental study and are detailed in Section IV.

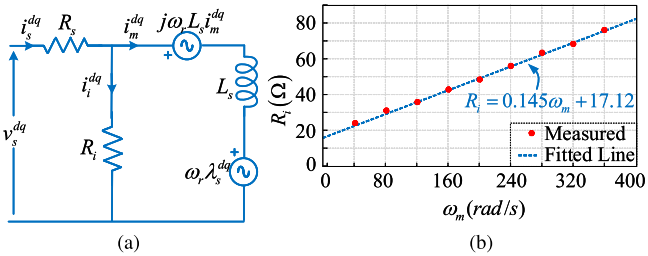

Fig. 1. (a) Equivalent circuit of PMBLDCM in dq-frame. (b) R_i at different ω_m.

II. Dynamics of PMBLDCM Considering Iron Loss

Let us consider the superscripts $\{a, b, c\}$ for the three phase quantities with 120° phase differences, superscripts $\{\alpha, \beta\}$ for stationary reference frame, and $\{d, q\}$ for direct and quadrature axes components in synchronously rotating reference frame. The abc-frame to $\alpha\beta$-frame and $\alpha\beta$-frame to dq-frame transformation are given in (1) using generic variable $X \in \{\text{voltage}(v), \text{current}(i), \text{back EMF}(e), \text{flux linkage}(\lambda)\}$

$$X^{\alpha\beta} = X^{\alpha} + jX^{\beta} = \sqrt{\frac{2}{3}} \sum_{\substack{k=1 \\ l\in\{a,b,c\}}}^{3} X^{l} e^{j\frac{2\pi}{3}(k-1)}$$
$$X^{dq} = X^{d} + jX^{q} = e^{-j\theta_r} X^{\alpha\beta} \tag{1}$$

where θ_r represents the rotor electrical position of PMBLDCM in rad. The equivalent circuit model of PMBLDCM in dq-plane is shown in Fig. 1(a) taking into account the iron losses. In steady state, the stator current (i_s^{dq}) of PMBLDCM can be represented in terms of the magnetizing (i_m^{dq}) and iron loss (i_i^{dq}) component as in the following equation:

$$i_s^{dq} = i_m^{dq} + i_i^{dq} = C^{-1} i_m^{dq} + \frac{\omega_r}{R_i} \lambda_s^{dq} \tag{2}$$

where $\lambda_s^{dq} = e_s^{dq}/\omega_m$ is the ratio of stator back EMF (e_s^{dq}) and motor angular speed (ω_m) in dq-frame, as shown in Fig. 2. The iron loss resistance (R_i) is calculated as per [31] and plotted as the linear approximation of the experimental data [see Fig. 1(b)].

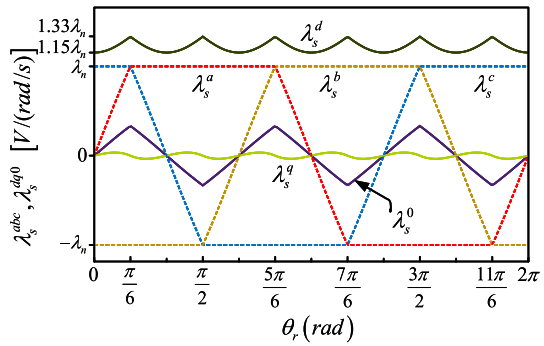

Fig. 2. Back EMF constant (λ_s) in abc and $dq0$-plane.

The effect of R_i corresponding to iron loss can be obtained as $C = k_c e^{-j\theta_c}$. The variables $k_c = 1/\sqrt{1+(\omega_r L_s/R_i)^2}$ and $\theta_c = \tan^{-1}(\omega_r L_s/R_i)$ are the magnitude and angle advancement due to inclusion of iron loss, respectively. ω_r is the rotor electrical speed and L_s is the stator inductance. From Fig. 1(a), the dynamics of the motor in dq-plane can be derived using (2), as given in the following equation:

$$\frac{di_s^{dq}}{dt} = -\left(\frac{C^{-1}}{\tau_s} + j\omega_r\right) i_s^{dq} + \frac{1}{L_s}\left(C^{-1}v_s^{dq} - e_s^{dq}\right) \tag{3}$$

where $\tau_s = L_s/R_s$ is the stator time constant with R_s as the stator resistance of PMBLDCM. Let $f_e^{dq} = -e_s^{dq}/L_s$ be the unknown disturbances in dq-plane, and $f_i^{dq} = -(C^{-1}/\tau_s + j\hat{\omega}_r)i_s^{dq}$ is the known disturbance calculated from the PMBLDCM parameters. $\hat{\omega}_r$ indicates the estimated value of ω_r. Now, the current model of the PMBLDCM in (3) can be represented as follows:

$$\frac{di_s^{dq}}{dt} = b_v v_s^{dq} + f_i^{dq} + f_e^{dq} \tag{4}$$

where $b_v = C^{-1}/L_s$ is the stator voltage (v_s^{dq}) control gain of the system. The electromagnetic torque (T_{em}) to be developed by the motor taking into account the iron loss component is given by the following equation:

$$T_{\text{em}} = \Re\left(\bar{\lambda}_s^{dq} i_m^{dq}\right) = \Re\left(C\bar{\lambda}_s^{dq} i_s^{dq}\right) - T_i \tag{5}$$

where $\bar{\lambda}_s^{dq}$ is the complex conjugate of λ_s^{dq}. In (5), if the iron loss effect is ignored, i.e., $C = 1$ and $T_i = 0$, then the torque $T_{\text{em}} = T_{\text{es}} = \Re(\bar{\lambda}_s^{dq} i_s^{dq}) = \lambda_s^d i_s^d + \lambda_s^q i_s^q$ can be obtained. The T_i is the additional electromagnetic torque component due to iron loss and its value varies with sectors from $S_1, \ldots, S_6$ as in the following equation:

$$T_i|_{S_1,\ldots,S_6} = \frac{\omega_m}{R_i}\left|\lambda_s^{dq}\right|^2_{S_1,\ldots,S_6}. \tag{6}$$

As T_{em} is a linear function of the q-axis current (i_s^q), the constant torque can be simply generated by controlling the q-axis current while keeping the d-axis current (i_s^d) at zero. However, applying this current to the PMBLDCM with nonsinusoidal back EMF ratio (λ_s^{dq}) will result in undesirable torque pulsations. Due to harmonic components in the back EMF, λ_s^d and λ_s^q will not be constant anymore and vary with respect to electric rotor position as depicted in Fig. 2. Considering the effect of iron loss with $i_s^d = 0$, the electromagnetic torque of (5) can be rewritten as follows:

$$T_{\text{em}} = k_t i_s^q - T_i \tag{7}$$

where $k_t = k_c|\lambda_s^{dq}|\sin(\theta_r + \theta_c)$ is the torque constant taking the effect of iron loss into consideration. Ignoring mechanical losses, PMBLDCM shaft torque is developed further from the electromagnetic torque T_{em} and expressed in terms of q-axis reference current (i_s^{q*}). Finally, the mechanical dynamics of PMBLDCM can be interpreted as follows:

$$\frac{d\omega_m}{dt} = \frac{1}{J}T_{\text{em}} - \frac{1}{J}T_L - \frac{B}{J}\omega_m = b_i i_s^{q*} + f_\omega^m \tag{8}$$

where $b_i = k_t/J$ is the current control gain of the system and $f_\omega^m = -(k_t(i_s^{q*} - i_s^q) + T_i + T_L + B\omega_m)/J$ is the total disturbance. T_L, J, and B are the load torque, moment of inertia, and damping coefficient of PMBLDCM, respectively.

III. ADRC-Based Sensorless Operation and Current Control Scheme Considering Iron Loss

This section provides estimation of rotor position along with high-performance current control scheme using two first-order ADRCs instead of conventional proportional-integral (PI) based speed and current controllers. The functional block diagram of these controllers and rotor position estimation is given in Fig. 3. The external speed ADRC is used as a speed regulator, supplying the i_s^{q*} to the internal current ADRC. The internal current ADRC is used to regulate the i_s^{dq} and track back EMF disturbance in order to reduce the motor torque ripple. In order to achieve such performances, following assumptions are considered.

1) Nonlinearities corresponding to saturation and deformities in PMBLDCM stator and rotor are considered as disturbances.
2) Disturbances and their derivatives (first and second) are uniformly bounded [22].
3) As the dynamic of the current loop is much faster than the speed loop, the current i_s^d is considered as "zero." The current i_s^q is bounded by a safety threshold as 2–3 times of the rated current of PMBLDCM.
4) Since the load torque variations influence the current directly, a large load torque change may violate the current constraint. Thus, it is reasonable to assume that the load torque T_L changes within a range related to i_s^q [21].

A. Linear ADRC-Based Current Controller Design

1) Current ADRC Design: The first-order perturbed system presented in (4) is considered for current ADRC design. The current i_s^x ($x \in \{d, q\}$) needs to be controlled with the control input v_s^x, where b_v is an estimate of input gain. Considering $\hat{f}_e^x$ as the estimated state of the PMBLDCM model, the current ADRC can be designed using LESO- and PLLO-based external disturbance observer as given in the following equations:

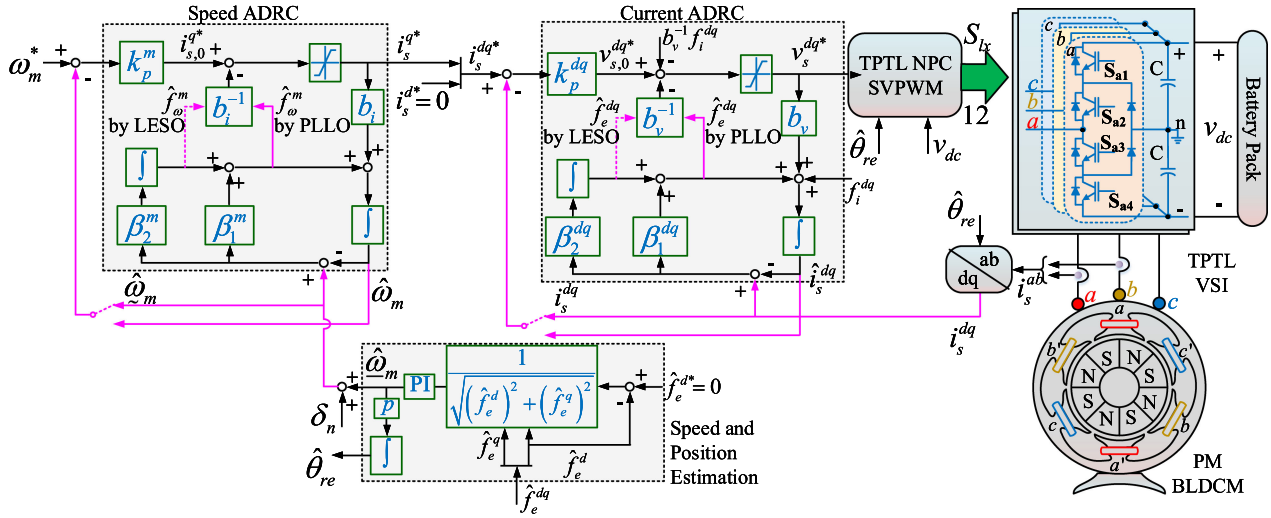

Fig. 3. Speed and current control of PMBLDCM using ADRC along with rotor position estimation.

1) LESO design:

$$\begin{cases} \dfrac{d\hat{i}_s^x}{dt} = b_v v_s^x + f_i^x + \hat{f}_e^x + \beta_1^x \varepsilon_i^x \\ \dfrac{d\hat{f}_e^x}{dt} = \beta_2^x \varepsilon_i^x, \quad x \in \{d, q\} \end{cases} \tag{9}$$

1) PLLO design:

$$\begin{cases} \dfrac{d\hat{i}_s^x}{dt} = b_v v_s^x + f_i^x + \hat{f}_e^x \\ \dfrac{d\hat{f}_e^x}{dt} = \beta_1^x \dfrac{d\varepsilon_i^x}{dt} + \beta_2^x \varepsilon_i^x \end{cases}, \quad x \in \{d, q\} \tag{10}$$

where $[\hat{i}_s^x, \hat{f}_e^x] \rightarrow [i_s^x, f_e^x]$ are the estimated stator current and unknown external disturbances in dq-plane, $\varepsilon_i^x = i_s^x - \hat{i}_s^x$ is the current estimation error. β_1^x and β_2^x are the observer gains needed to be evaluated from the error margins and system stability criteria. According to the ADRC theory [32], the estimated external disturbance can be used as a feed-forward compensation term for the input of PMBLDCM. Therefore, the final control law of the PMBLDCM can be designed as follows:

$$v_s^x = v_{s,0}^x - b_v^{-1}\left(f_i^x + \hat{f}_e^x\right) \tag{11}$$

where $v_{s,0}^x$ is the plant input generated by the initial control law. Substituting (11), the perturbed system in (4) is reduced to

$$\frac{di_s^x}{dt} = b_v v_{s,0}^x. \tag{12}$$

2) Stability and Tracking Performance Analysis: Desired closed-loop performance is achieved by selecting a simple proportional current controller as feedback controller and is given by

$$v_{s,0}^x = k_p^x \left(i_s^{x*} - i_s^x\right), \quad x \in \{d, q\} \tag{13}$$

where k_p^x is the proportional gain of the controller and is determined as a tradeoff between the steady-state and transient performance. The transfer function given in (14) relates the estimated disturbance $\hat{f}_e^x$ to the commanded disturbance f_e^x with the characteristics polynomial of $(s^2 + \beta_1^x s + \beta_2^x)$. The obtained polynomial is further compared with the second-order undamped system $((s + \omega_o^x)^2)$, where ω_o^x is the undamped natural frequency. The basis of this parameterization is to assign all the observer eigenvalues at $-\omega_o^x$

$$\frac{\hat{f}_e^x(s)}{f_e^x(s)} = \begin{cases} \frac{\beta_2^x}{s^2+\beta_1^x s+\beta_2^x} & \text{using LESO} \\ \frac{\beta_1^x s+\beta_2^x}{s^2+\beta_1^x s+\beta_2^x} & \text{using PLLO} \end{cases}, \quad x \in \{d, q\}. \tag{14}$$

The stability of the current ADRC is tested at observer bandwidth of $\beta_1^x = 2\omega_o^x$. The gain value $\beta_2^x = (\omega_o^x)^2$ provides the natural frequency of both the observer. The bandwidth of the LESO should be kept large enough to ensure a faster dynamic tracking of disturbance variation which is observed from Fig. 4(a). At this condition, the sensitivity to the sensor noises and the delay in sampling must be acceptable. Comparing with Fig. 4(b), it can be concluded that the desired performance in case of PLLO can be achieved at almost half the bandwidth of the LESO model. In order to evaluate the steady-state response of the current ADRC, the error transfer function of the disturbance $(\Phi_e^x(s))$ can be obtained as in the following equation:

$$\Phi_e^x(s) = \frac{f_e^x(s) - \hat{f}_e^x(s)}{f_e^x(s)} = \begin{cases} \frac{s(s+\beta_1^x)}{s^2+\beta_1^x s+\beta_2^x} & \text{using LESO} \\ \frac{s^2}{s^2+\beta_1^x s+\beta_2^x} & \text{using PLLO.} \end{cases} \tag{15}$$

Under a ramp-change excitation (with a slope of 75) of the commanded f_e^x, the time/frequency-domain response of the external disturbance estimation error is obtained, according to (15). A frequency-domain analysis is provided with magnitude and phase of $\Phi_e^x(s)$ at various ω_o^x changing from 50 to 450 rad/s with an increment of 20 rad/s, as shown in Fig. 4(a) and (b). In addition, a time-domain characteristic in Fig. 4(c) provides the information on selection of the bandwidth considering the steady-state error. The results in Fig. 4 show that the bandwidth of the PLLO has a significant impact on the disturbance estimation accuracy than LESO. At increasing bandwidth, the disturbance estimation error decreases, and the tracking speed increases. After selecting the accurate ω_o^x, the parameter k_p^x is

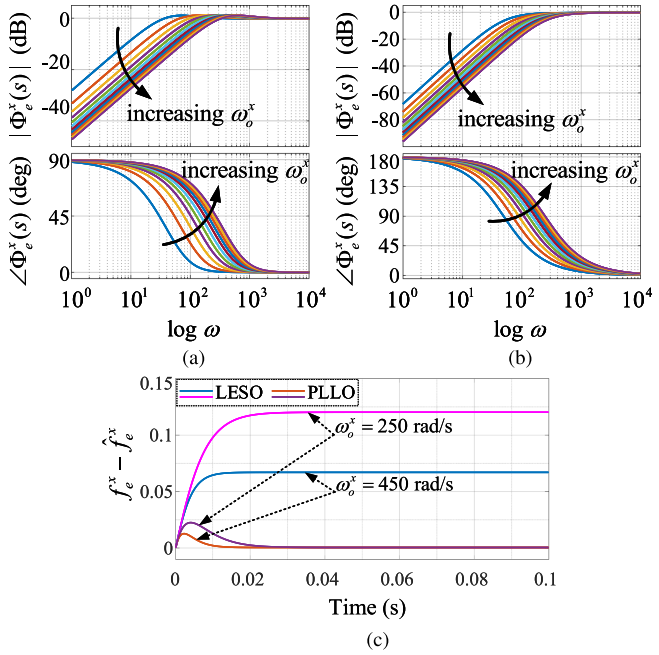

Fig. 4. Bode diagram of $\Phi_e^x(s)$ for (a) LESO and (b) PLLO. (c) Time plot of $f_e^x(s) - \hat{f}_e^x(s)$ for LESO and PLLO of current ADRC.

chosen to be 20%–33% of ω_o^x for improved performance of current ADRC [33]. This approximation is valid only when k_p^x is determined particularly by the settling time specification of the transient response.

B. ADRC-Based Accurate Speed Estimation and Control

1) Sensorless Operation: This section presents an estimation of rotor position and the motor speed from the estimated disturbances $\hat{f}_e^{dq}$ corresponding to back EMF in dq-plane, as shown in Fig. 3. The estimated q-axis unknown external disturbance $\hat{f}_e^q$ contains the rotor position error information and, thus, needs to be normalized for further estimation process. A tracking controller with a PLL is used to regulate the normalized $\hat{f}_e^d$ to zero. The estimated back EMF normalization ensures a constant linear dynamic response of the tracking controller regardless of the fundamental operating frequency. Comparing with the conventional back EMF based rotor position estimation, this proposed method removes the need of LPF and eliminates the phase delay corresponding to complex cutoff frequency selection process. Furthermore, the proposed estimation method uses a synchronously rotating frame instead of stationary reference frame for the implementation of flat/linear ADRC.

2) Speed ADRC Design: The estimated speed $\hat{\omega}_m$ is given as feedback along with additional measurement noise δ_n to the first-order perturbed system presented in (8). A LESO- and PLLO-based external disturbance observer for speed controller can be designed as given in the following equations:

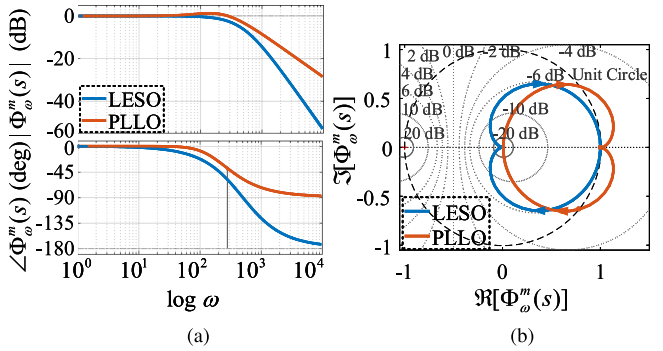

Fig. 5. Speed ADRC. (a) Bode diagram and (b) Nyquist plot for $\Phi_\omega^m(s)$ using LESO ($\omega_o^m = 500$ rad/s) and PLLO ($\omega_o^m = 200$ rad/s).

2) LESO design:

$$\begin{cases} \dfrac{d\hat{\omega}_m}{dt} = b_i i_s^{q*} + \hat{f}_\omega^m + \beta_1^m \varepsilon_\omega^m \\ \dfrac{d\hat{f}_\omega^m}{dt} = \beta_2^m \varepsilon_\omega^m \end{cases} \tag{16}$$

2) PLLO design:

$$\begin{cases} \dfrac{d\hat{\omega}_m}{dt} = b_i i_s^{q*} + \hat{f}_\omega^m \\ \dfrac{d\hat{f}_\omega^m}{dt} = \beta_1^m \dfrac{d\varepsilon_\omega^m}{dt} + \beta_2^m \varepsilon_\omega^m \end{cases} \tag{17}$$

where $[\hat{\omega}_m, \hat{f}_\omega^m] \rightarrow [\omega_m, f_\omega^m]$ are the estimated mechanical angular speed of the motor and unknown total disturbances, $\varepsilon_\omega^m = \omega_m - \hat{\omega}_m$ is the observing speed estimation error.

3) Stability and Tracking Performance Analysis: The reference speed can be tracked down using a simple linear feedback control law as in (13). Hence, the closed-loop transfer function of the speed controller, while choosing $****\hat{\omega}_m$ or $\hat{\omega}_m$ as the speed feedback, can be derived as follows:

$$\frac{\omega_m(s)}{\omega_m^*(s)} = \frac{b_i k_p^m}{s + b_i k_p^m}. \tag{18}$$

To ensure the tracking efficiency of the ADRC, a timely and appropriate estimate of external disturbance is necessary. The frequency-domain transfer function between the estimated value $\hat{f}_\omega^m(s)$ and the actual value $f_\omega^m(s)$ of the external disturbance can be obtained as given in (19). By choosing $\beta_1^x = 2\omega_o^m$ and $\beta_2^x = (\omega_o^m)^2$, the characteristic polynomial of LESO/PLLO can be expressed as $s^2 + \beta_1^m s + \beta_2^m = (s + \omega_o^m)^2$, where ω_o^m is the undamped natural frequency of speed observer

$$\Phi_\omega^m(s) = \frac{\hat{f}_\omega^m(s)}{f_\omega^m(s)} = \begin{cases} \frac{\beta_2^m}{s^2+\beta_1^m s+\beta_2^m} & \text{using LESO} \\ \frac{\beta_1^m s+\beta_2^m}{s^2+\beta_1^m s+\beta_2^m} & \text{using PLLO.} \end{cases} \tag{19}$$

To achieve desired speed control loop stability, ω_o^m is set to 500 and 200 rad/s in LESO and PLLO, respectively. It is evaluated using a similar approach provided in Fig. 4(c). In order to analyze disturbance rejection and noise suppression for speed ADRC, bode diagram and Nyquist plot with LESO and PLLO are shown in Fig. 5(a) and (b), respectively. Comparing the speed ADRC performance using LESO and PLLO, the PLLO provides a better

TABLE I
PARAMETERS FOR SIMULATION AND EXPERIMENT

Simulation and hardware PMBLDCM parameters
3Φ, 8 Pole, V_{dc}=240V, $P_{rated} = 2.5\,kW$, $\omega_{rated} = 1500\,rpm$, $T_{rated} = 20N.m$, $\lambda_n = 0.175\,V.s/rad$, $R_s = 2.4\,\Omega$, $L_s = 8.5\,mH$, $J = 0.089Kg.m^2$, $B = 10^{-3}N.m.s/rad$.
Simulation and hardware controller parameters
Sample time, $T_s = 10\,\mu s$, Switching Frequency, $f_{sw} = 5\,kHz$, Dead time, $t_d = 1\,\mu s$, $k_p^d = 95$, $k_p^q = 115$ (for both LESO and PLLO), k_p^m (LESO)= 98.5, k_p^m (PLLO)=52.6

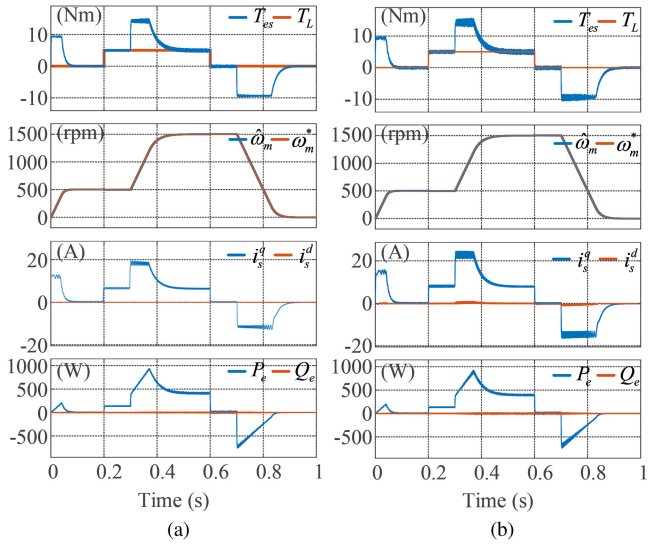

Fig. 6. Simulation results of $T_{\rm es}$, $\hat{\omega}_m$, i_s^d, i_s^q, P_e, and Q_e for (a) MTPA-ADRC and (b) MTPA-DTC while positive speed change, loading, unloading, and negative speed change.

disturbance rejection property at low frequency when the noise suppression performance of both systems is similar. When the disturbance rejection properties of both observers are identical, the LESO contributes an enhanced noise suppression capability as the noise is mostly high frequency.

IV. RESULTS AND DISCUSSIONS

The PMBLDCM drive system shown in Fig. 3 consists of a TPTL-NPC VSI and a dynamometer coupled PMBLDCM. The proposed sensorless speed ADRC and current ADRC are verified both through simulation study as well as experimental results. The parameters for both the simulation and hardware prototypes are listed in Table I. The dc voltage is derived from 240 V, 1000 Ah battery back.

A. Simulation Results

The PMBLDCM drive is simulated using MATLAB/Simulink to compare the performance of the MTPA-ADRC and MTPA-DTC. The simulation results of $T_{\rm es}$, load torque (T_L), $\hat{\omega}_m$, ω_m^*, i_s^q, i_s^d, active and reactive power (P_e, Q_e) under different disturbances such as positive step change in speed, positive step change in load, negative step change in load, and negative step change in speed are shown in Fig. 6(a) and (b), respectively. At $t = 0$ s, the motor is commanded with speed of $\omega_m^* = 500$ r/min

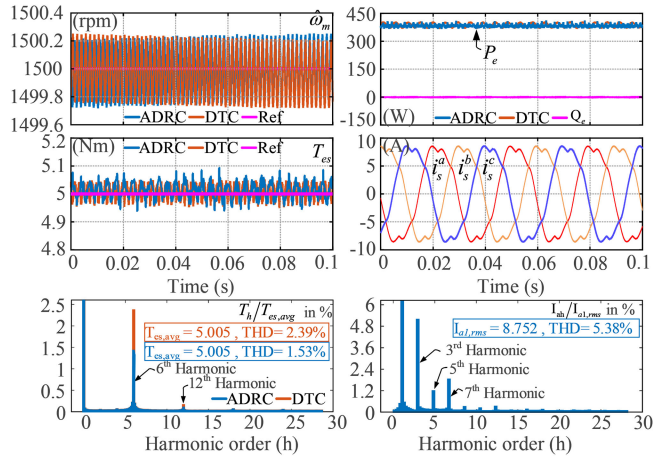

Fig. 7. Simulation results: Expanded view of $\hat{\omega}_m$, $T_{\rm es}$, P_e, Q_e, i_s^{abc}, and harmonic analysis of $T_{\rm es}$ and i_s^{abc} at steady-state drive operation.

at no load. Due to inertia, PMBLDCM approaches the steady-state speed at $t = 0.07$ s. A step change in load torque of $T_L = 5$ N.m is given at $t = 0.2$ s. The proposed sensorless speed ADRC responds instantly and accurately estimates the speed during load change. Such performance is compared with MTPA-DTC which provides faster dynamic but with higher torque ripple in comparison to the proposed one. A step change in ω_m^* from 500 to 1500 r/min with a load of $T_L = 5$ N.m is given at $t = 0.3$ s. The PMBLDCM takes 0.17 s to reach steady state. During speed transition, PMBLDCM reaches its maximum torque and power requirement. It is also observed that proposed MTPA-ADRC has lower torque ripple during the speed transition compared to MTPA-DTC. The i_s^q follows the torque requirement by nullifying i_s^d. With steady-state speed of 1500 r/min, PMBLDCM is unloaded in order to investigate the response of the proposed sensorless ADRC scheme. After unloading, a slight increase in $\hat{\omega}_m$ is observed with both the controllers. However, $\hat{\omega}_m$ settles faster with the MTPA-ADRC than the MTPA-DTC. At $t = 0.7$ s, a negative step change in ω_m^* from 1500 to 0 r/min is commanded as shown in Fig. 6(a) and (b). The PMBLDCM achieves zero speed after 0.17 s. During the reduction in speed, a regenerative action is also observed in both the methods. The proposed speed ADRC and current ADRC scheme possesses faster dynamic since speed tracks the reference with minimal steady-state errors and satisfactory transient response.

The performance results of $\hat{\omega}_m$, ω_m^*, T_{es}, T_L, P_e, Q_e for MTPA-ADRC and MTPA-DTC during steady state is provided in Fig. 7 with harmonic spectra of $T_{\rm es}$ and $i_s^{a,b,c}$. The active power demand matches the dynamics of torque developed and the zero reactive power resulting in reduced losses. The 6th and 12th harmonics in $T_{\rm es}$ are 2.3% and 0.1%, respectively. $T_{\rm es}$ comprises 1.53 %THD with MTPA-ADRC and 2.39 %THD with MTPA-DTC. This indicates that the proposed MTPA-ADRC has lower torque ripple in comparison to MTPA-DTC. In addition, MTPA-ADRC shows a steady-state error of only 0.015%. The stator current waveform is following the petal-wave current

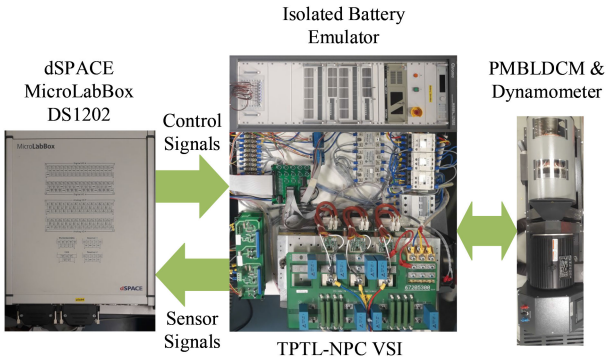

Fig. 8. PMBLDCM hardware prototype.

pattern with THD of 5.83% which is significantly lower than the conventional quasi-square wave current pattern.

B. Experimental Verification and Results

Fig. 8 shows the picture of the experimental prototype test-bench. PMBLDCM is coupled to a dc machine operated dynamometer. The digital controller DS1202 is used to implement the control algorithms. An isolated battery emulator is used to power the TPTL-NPC VSI. In order to minimize the sensor requirement, only two current sensors (LEM LA55P) and one voltage sensor (LEM LV25P) are used for the measurement of two-phase stator current (i_s^{ab}) and battery voltage ($v_{\rm dc}$), respectively. The other phase current can be obtained as $i_s^c = -(i_s^a + i_s^b)$ considering balanced PMBLDCM supply. The three-phase voltages are calculated from $v_{\rm dc}$ and the switching function "S_{lx}" by using the relation $v_s^l = [S_{l1}\&S_{l2}\ S_{l2}\&S_{l3}\ S_{l3}\&S_{l4}][\,v_{\rm dc}/2\ 0\ -v_{\rm dc}/2]^t,\ l \in \{a,b,c\}$. The motor torque, speed, active, and reactive power demand along with dq-plane stator current is estimated in real time and are accessed using digital-to-analog converter (DAC) ports of the controller.

The experimentally acquired waveforms of $T_{\rm es}$, $\hat{\omega}_m$, i_s^{dq}, P_e, Q_e, $i_{\rm bat}$, and i_s^{abc} under different operating conditions are given for 1) proposed sensorless MTPA-ADRC taking iron loss into account in Fig. 9 and 2) MTPA-DTC strategy ignoring iron loss as per [12] in Fig. 10. In both cases, identical controller parameters such as sampling time ($T_s = 10\,\mu$s) and switching frequency ($f_{\rm sw} = 5$ kHz) are maintained. The PMBLDCM is accelerated from stand still to 500 r/min at t_1 with a step speed command under no load. The motor speed reaches its steady state in 70 ms in the case of proposed MTPA-ADRC and settles faster than the MTPA-DTC. At t_2 (i.e., steady state), T_L of 5 N.m is applied without any fluctuation in $\hat{\omega}_m$ which proves the faster dynamics of sensorless speed ADRC. A step speed command of 1000 r/min is given at t_3, while the motor is loaded and the speed settles at 1500 r/min in 170 ms. During the speed transition, the active power P_e demand follows the torque requirement and the reactive power Q_e remains constant at zero verifying that the phase current and phase back EMF are in phase. It can be observed that sudden load removal at t_4 does not affect motor speed response. At t_5, both the controllers perform a regenerative action by detecting a negative change in speed, and, finally, the PMBLDCM achieves zero speed at t_6.

The time scale expanded results of $i_{\rm bat}$ and i_s^{abc} at steady state for $\hat{\omega}_m = 500$ r/min and $\hat{\omega}_m = 1500$ r/min with load torque of 5 N.m are presented for the proposed model with loss in Fig. 9(c) and the model without iron loss [12] in Fig. 10(c), respectively. These plots show less ripple for the proposed MTPA-ADRC algorithm. The hardware results for PMBLDCM at rated load and rated speed are shown in Fig. 11. The drive performances for the proposed MTPA-ADRC and MTPA-DTC are reported in Fig. 11(a) and (b), respectively, for the comparative study. The motor is initially given a load of 0–5 N.m at $t = t_1$ s, while the drive system is not yet enabled to operate. A speed command of 1500 r/min at t_2 s is provided to the motor. The torque requirement becomes high during the speed transition period and it settles to its commanded value once the drive achieves the stable condition. It can be clearly observed that with the proposed MTPA-ADRC and MTPA-DTC, the durations to achieve the stable condition are 70 and 80 ms, respectively. Thereby, the comparative study from Fig. 11(a) and (b) reveals that the proposed algorithm gives faster response with reduced ripple. Further, at $t = t_3$ s, a load of $T_L = 20$ N.m is given to PMBLDCM drive system although the speed remains unchanged, which demonstrates the effective performance of the proposed approach. Moreover, the PMBLDCM is tested at low speed and speed reversal to investigate the stability of the drive system. The hardware performances for the proposed MTPA-ADRC and existing MTPA-DTC at low speed and speed reversal are shown in Fig. 12(a) and (b), respectively.

Lissajous curves of $e_s^{\alpha\beta}$ and $i_s^{\alpha\beta}$ for the proposed MTPA-ADRC are presented in Fig. 13. Fig. 13(a) and (b) illustrates the Lissajous pattern at $\hat{\omega}_m = 1500$ r/min with the delivered load of $T_L = 20$ and 5 N.m, respectively. The PMBLDCM drive system has also been tested at lower speed, i.e., $\hat{\omega}_m = 300$ r/min at $T_L = 5$ N.m, and the Lissajous pattern is shown in Fig. 13(c). With this experimental investigation, a trapezoidal phase back EMF and a petal-wave current pattern are truly achieved which match the analytical descriptions. The stator phase current waveform appears like petal-wave with low ripple for the proposed MTPA-ADRC method which validates the theoretical observations. The experimentally computed THD values of i_s^a and $T_{\rm es}$ are shown in Fig. 14(a) and (b), respectively, for $T_L = 5$ N.m. These results are in agreement with the corresponding simulation results shown in Fig. 7. The harmonic analysis of motor torque shows THD of 2.39% where 6th and 12th harmonics are dominant with magnitude of 2.3% and 0.1%, respectively. The comparative ripple values of $T_{\rm es}$, $\hat{\omega}_m$, P_e, i_s^{dq}, and $i_{\rm bat}$ computed from the experimental results are tabulated in Table II. The last column in Table II shows the improvement in the ripple in $T_{\rm es}$, $\hat{\omega}_m$, P_e, i_s^{dq}, and $i_{\rm bat}$. These comparative results demonstrate the significant reduction in ripple of various parameters by the proposed MTPA-ADRC method with iron loss when compared with that of MTPA-DTC [12], where iron losses are neglected, thus validating the analytical observations.

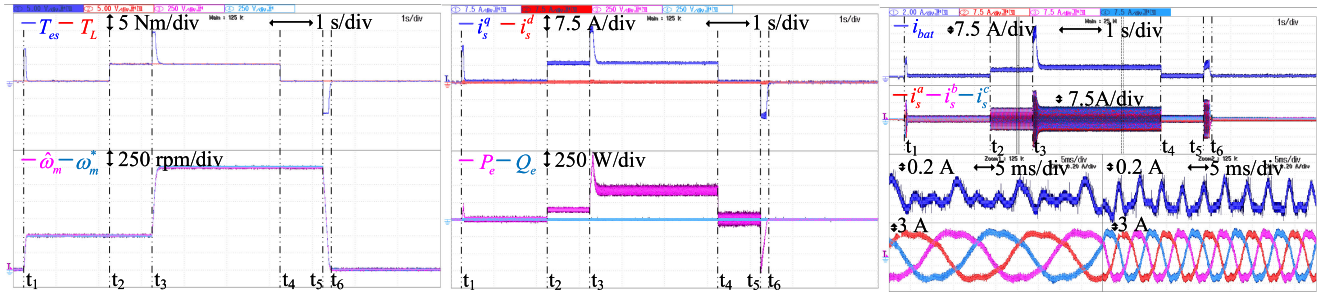

Fig. 9. Experimental results of (a) T_{es}, $\hat{\omega}_m$ (b) i_s^{dq}, P_e, and Q_e and (c) i_{bat} and i_s^{abc} for the proposed MTPA-ADRC.

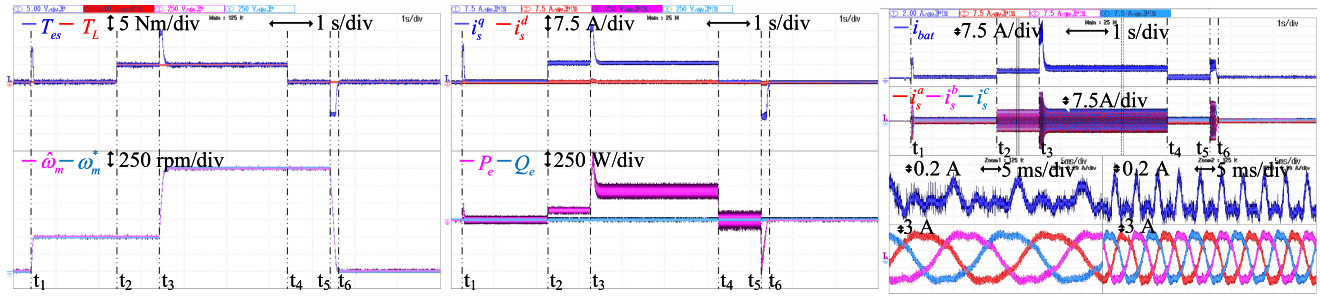

Fig. 10. Experimental results of (a) T_{es}, $\hat{\omega}_m$ (b) i_s^{dq}, P_e, and Q_e and (c) i_{bat} and i_s^{abc} for MTPA-DTC [12].

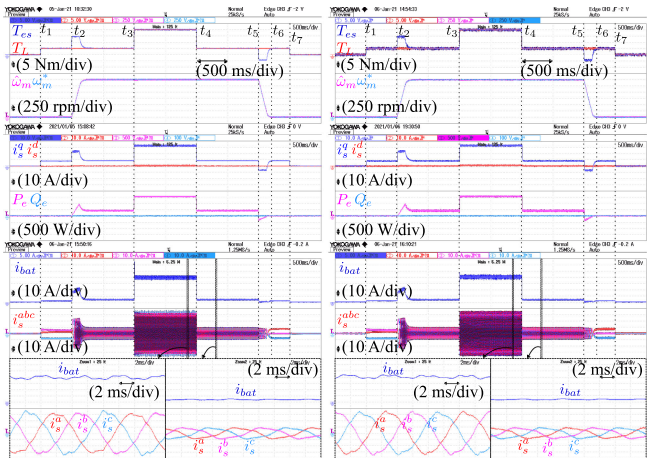

Fig. 11. Hardware results: Rated load and rated speed operation for (a) MTPA-ADRC and (b) MTPA-DTC controlled PMBLDCM drive.

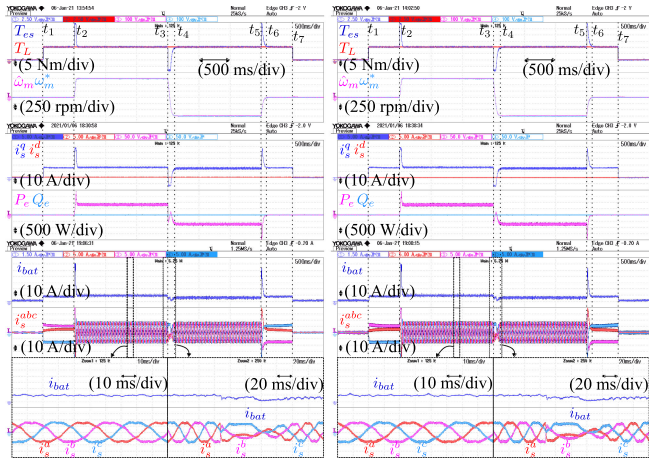

Fig. 12. Hardware results: Low speed and speed reversal operation for (a) MTPA-ADRC and (b) MTPA-DTC controlled PMBLDCM drive.

TABLE II
RIPPLE % COMPARISON FOR THE PROPOSED MTPA-ADRC WITH MTPA-DTC [R_3] AT (I) 300, (II) 500, AND (II) 1500 R/MIN

Parameters (in %)	MTPA-ADRC			MTPA-DTC [R_3]			% Improvement		
	$300rpm$	$500rpm$	$1500rpm$	$300rpm$	$500rpm$	$1500rpm$	$300rpm$	$500rpm$	$1500rpm$
ΔT_{es}	2.9	3.1	3.5	6.7	6.9	7.6	56.7	55. 07	53.9
$\Delta\hat{\omega}_m$	2.9	3.1	7.4	4.3	4.6	12.6	32.5	32.6	41.2
ΔI_s^{dq}	2.4	2.6	4.9	6.5	6.8	7.8	63.07	61.7	37.1
ΔP	1.2	1.4	2.8	2.9	3.1	9.4	58.6	54.8	70.2
Δi_{bat}	8.9	9.2	12.1	10.9	11.1	14.1	18.3	17.1	14.1
η	73.6	82.6	95.2	72.3	81.7	94.8	1.8	0.73	0.42

C. Tracking Error and Sensorless Speed Estimation

The experimental result for speed tracking error is provided to validate the robustness to the estimated disturbances using the proposed ADRC-based sensorless operation. The tracking error of the estimated speed using LESO and PLLO at $\hat{\omega}_m = 1500$ r/min is depicted in Fig. 15(a) and (b), while an external disturbance is applied at $t = t_x$ s. The $\hat{\omega}_m$ approaches the commanded speed ω_m^* with an estimation error ε_ω^m, as shown in Fig. 15(a) (middle) and (b) (middle). It can be observed that

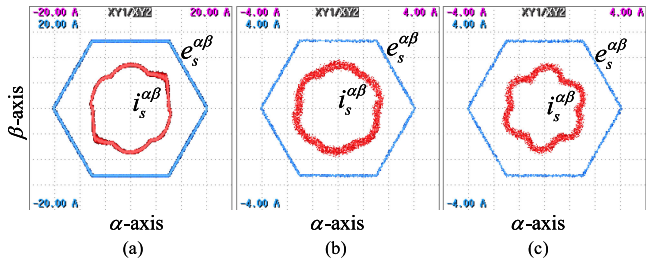

Fig. 13. Trajectories of $e_s^{\alpha\beta}$ and $i_s^{\alpha\beta}$ for the proposed MTPA-ADRC at various operating conditions. (a) $\hat{\omega}_m = 1500$ r/min, $T_L = 20$ N.m. (b) $\hat{\omega}_m = 1500$ r/min, $T_L = 5$ N.m. (c) $\hat{\omega}_m = 300$ r/min, $T_L = 5$ N.m.

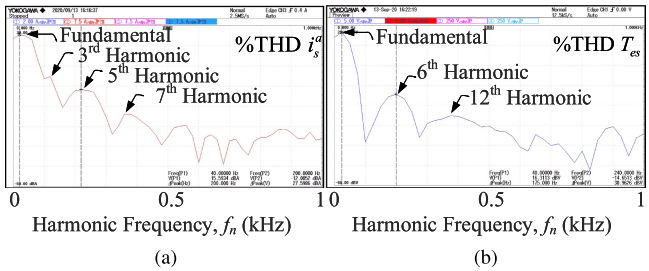

Fig. 14. Experimental results at $\hat{\omega}_m = 1500$ r/min, and $T_L = 5$ N.m. (a) %THD i_s^a and (b) %THD T_{es} for the proposed MTPA-ADRC with iron loss.

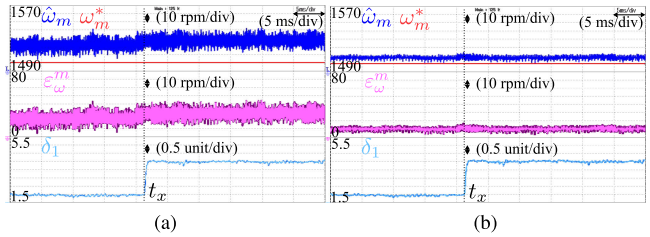

Fig. 15. Hardware results: tracking error of the estimated rotor speed for MTPA-ADRC with (a) LESO and (b) PLLO at $\hat{\omega}_m = 1500$ r/min with variation in disturbance δ_1 at t_x.

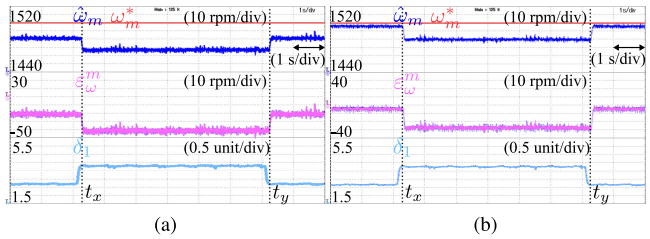

Fig. 16. Hardware results: tracking error of the estimated rotor speed for MTPA-ADRC with (a) LESO and (b) PLLO at $\hat{\omega}_m = 1500$ r/min with change in T_L from 5 to 20 N.m at t_x and again to 5 N.m at t_y.

the speed tracking error using the PLLO is 25% lower than the LESO due to better disturbance rejection property of PLLO. The moment when disturbances increase, the deviation in estimated speed and speed error also increases. The ripple in the estimated speed is found to be lower with PLLO rather than LESO. Similar observation is also made in Fig. 16 by changing the load from 5 to 20 N.m at t_x and again to 5 N.m at t_y. Again, it is observed that PLLO provides speed estimation with lower ripple and reduced tracking error in comparison to LESO.

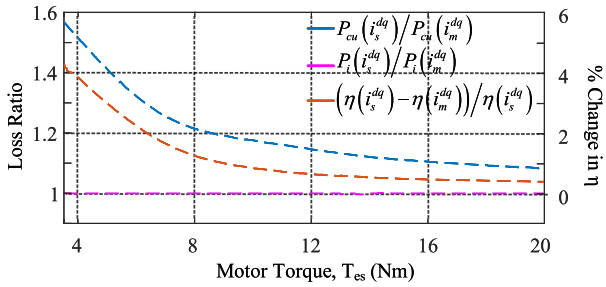

Fig. 17. Loss ratio and % change in η curve with respect to load variation at 1500 r/min.

D. Power Loss and Efficiency Analysis

The iron loss ($P_i = P_{\text{in}} - 3R_s(I_s^{\text{rms}})^2$) obtained from steady-state no-load test is regarded as the losses due to both eddy current (P_{ed}) and hysteresis (P_h). The input power (P_{in}) of PMBLDCM with root mean square (rms), phase voltage (V_s^{rms}), and phase current (I_s^{rms}) is measured using a power analyzer. The no-load speed is measured using a tachometer. From the analytical expression in (20), it is observed that the iron loss P_i is directly proportional to the ω_r^2 as P_{ed} is significantly high for PMBLDCM

$$P_i = P_h + P_{ed} = \frac{\left|e_s^{dq}\right|^2}{R_h} + \frac{\left|e_s^{dq}\right|^2}{R_e} = \frac{k\omega_r\left|\lambda_s^{dq}\right|^1.6}{R_e} + \frac{\omega_r^2\left|\lambda_s^{dq}\right|^2}{R_e} \tag{20}$$

where R_i is the effective iron loss resistance corresponding to parallel combination of eddy current resistance (R_e) and hysteresis loss resistance (R_h). It is observed that the iron loss corresponding to i_s^{dq} ($P_i(i_s^{dq})$) is almost equal to the iron loss corresponding to i_m^{dq} ($P_i(i_m^{dq})$). The iron loss ratio $P_i(i_s^{dq})/P_i(i_m^{dq})$ is illustrated in Fig. 17. Since the stator current i_s^{dq} is larger than the i_m^{dq}, the copper loss ($P_{\text{cu}}(i_s^{dq})$) considering the iron loss effect is higher than the copper loss ($P_{\text{cu}}(i_m^{dq})$) corresponding to lossless model of PMBLDCM. The copper loss ratio of $P_{\text{cu}}(i_s^{dq})$ and $P_{\text{cu}}(i_m^{dq})$ is shown in Fig. 17

$$\begin{aligned} P_{\text{cu}}\left(i_s^{dq}\right) &= \tfrac{3}{\pi}\textstyle\int_{S_1\ldots S_6} R_s\left|i_s^{dq}\right|^2 d\hat{\theta}_r \\ P_{cu}\left(i_m^{dq}\right) &= \tfrac{3}{\pi}\textstyle\int_{S_1\ldots S_6} R_s\left|i_m^{dq}\right|^2 d\hat{\theta}_r. \end{aligned} \tag{21}$$

The efficiency (η) of PMBLDCM can be evaluated by the relation $\eta = \frac{P_e}{P_{\text{in}}} \times 100\%$. The % change in η with/without considering the effect of iron loss ($\eta(i_s^{dq}), \eta(i_m^{dq})$) is shown in Fig. 17. It can be observed that the % change in η has negligible effect at the rated condition of the drive operation. The % change in η at $\hat{\omega}_m = 300$, 500, and 1500 r/min and $T_L = 5$ N.m are quantified in Table II for MTPA-ADRC and MTPA-DTC methods. It is concluded that significant improvement in efficiency is achieved at low speed condition for the proposed MTPA-ADRC scheme.

V. Conclusion

A linear ADRC-based speed and current control scheme considering the iron loss effect is proposed for the PMBLDCM drives. Both the control schemes are demonstrated with two different observers, i.e., LESO and PLLO. Speed ADRC tracks the commanded speed precisely by comparing a sensorless

speed feedback approximation. Moreover, the current ADRC provides an accurate disturbance estimation corresponding to the back EMF with optimized modulation control. The effect of iron loss on MTPA control is also implemented in order to enhance the drive efficiency by reducing both copper loss and iron loss. The proposed algorithm involves an estimation of the total disturbance that aims to reduce design and execution complexity, particularly in the higher order model. The improved drive performance with the proposed approach is demonstrated analytically and compared with the current research without regard to the internal disturbance effect. The motor currents in the stationary reference frame show a petal-wave Lissajous pattern resulting in less ripple and, thus, reduced copper losses and smooth motor torque. The performance of the proposed MTPA-ADRC control drive is compared with that of the MTPA-DTC drive both by simulation and laboratory experiments. The comparative results show the improved performance of the proposed algorithms. The proposed algorithm for sensorless PMBLDCM drive will find application in high performance applications and electric transportation. Improving the proposed ADRC with online estimation of motor parameters will be an interesting research work for the future.

References

[1] F. Naseri, E. Farjah, and T. Ghanbari, "An efficient regenerative braking system based on battery/supercapacitor for electric, hybrid, and plug-in hybrid electric vehicles with BLDC motor," *IEEE Trans. Veh. Technol.*, vol. 66, no. 5, pp. 3724–3738, May 2017.

[2] L. Yang, Z. Q. Zhu, H. Bin, and L. Gong, "Spectral analysis and sideband harmonic cancellation of six-step operation with low carrier-fundamental frequency ratio for high-speed brushless DC drives," *IEEE Trans. Ind. Electronics, early access*, 2020. doi: 10.1109/TIE.2020.3018069.

[3] D. Zhao, X. Wang, B. Tan, L. Xu, C. Yuan, and Y. Huangfu, "Fast commutation error compensation for BLDC motors based on virtual neutral voltage," *IEEE Trans. Power Electron.*, vol. 36, no. 2, pp. 1259–1263, Feb. 2021.

[4] Y. Li, X. Song, X. Zhou, Z. Huang, and S. Zheng, "A sensorless commutation error correction method for high-speed BLDC motors based on phase current integration," *IEEE Trans. Ind. Inform.*, vol. 16, no. 1, pp. 328–338, Jan. 2020.

[5] H. K. Samitha Ransara and U. K. Madawala, "A torque ripple compensation technique for a low-cost brushless DC motor drive," *IEEE Trans. Ind. Electron.*, vol. 62, no. 10, pp. 6171–6182, Oct. 2015.

[6] A. G. de Castro, W. C. A. Pereira, T. E. P. de Almeida, C. M. R. de Oliveira, J. R. B. de Almeida Monteiro, and A. A. de Oliveira, "Improved finite control-set model-based direct power control of BLDC motor with reduced torque ripple," *IEEE Trans. Ind. Appl.*, vol. 54, no. 5, pp. 4476–4484, Oct. 2018.

[7] M. Fasil, N. Mijatovic, B. B. Jensen, and J. Holboll, "Nonlinear dynamic model of PMBLDC motor considering core losses," *IEEE Trans. Ind. Electron.*, vol. 64, no. 12, pp. 9282–9290, Dec. 2017.

[8] A. Dadashnialehi, A. Bab-Hadiashar, Z. Cao, and A. Kapoor, "Intelligent sensorless antilock braking system for brushless in-wheel electric vehicles," *IEEE Trans. Ind. Electron.*, vol. 62, no. 3, pp. 1629–1638, Mar. 2015.

[9] L. Yang, J. Zhao, X. Liu, A. Haddad, J. Liang, and H. Hu, "Effects of manufacturing imperfections on the circulating current in ironless brushless DC motors," *IEEE Trans. Ind. Electron.*, vol. 66, no. 1, pp. 338–348, Jan. 2019.

[10] P. Kshirsagar and R. Krishnan, "High-efficiency current excitation strategy for variable-speed nonsinusoidal back-EMF PMSM machines," *IEEE Trans. Ind. Appl.*, vol. 48, no. 6, pp. 1875–1889, Dec. 2012.

[11] G. Buja, M. Bertoluzzo, and R. K. Keshri, "Torque ripple-free operation of PM BLDC drives with petal-wave current supply," *IEEE Trans. Ind. Electron.*, vol. 62, no. 7, pp. 4034–4043, Jul. 2015.

[12] A. Khazaee, H. Abootorabi, G. Arab Markadeh, and H. Mosaddegh, "MTPA strategy for direct torque control of brushless DC motor drive," *IEEE Trans. Ind. Electron., early access*, 2020. doi: 10.1109/TIE.2020.3009576.

[13] S. J. Park, H. W. Park, M. H. Lee, and F. Harashima, "A new approach for minimum-torque-ripple maximum-efficiency control of BLDC motor," *IEEE Trans. Ind. Electron.*, vol. 47, no. 1, pp. 109–114, Feb. 2000.

[14] C. Lai, G. Feng, J. Tjong, and N. C. Kar, "Direct calculation of maximum-torque-per-ampere angle for interior PMSM control using measured speed harmonic," *IEEE Trans. Power Electron.*, vol. 33, no. 11, pp. 9744–9752, Nov. 2018.

[15] K. Li and Y. Wang, "Maximum torque per ampere (MTPA) control for IPMSM drives based on a variable-equivalent-parameter MTPA control law," *IEEE Trans. Power Electron.*, vol. 34, no. 7, pp. 7092–7102, Jul. 2019.

[16] A. Shinohara, Y. Inoue, S. Morimoto, and M. Sanada, "Direct calculation method of reference flux linkage for maximum torque per ampere control in DTC-based IPMSM drives," *IEEE Trans. Power Electron.*, vol. 32, no. 3, pp. 2114–2122, Mar. 2017.

[17] K. Xia, Y. Ye, J. Ni, Y. Wang, and P. Xu, "Model predictive control method of torque ripple reduction for BLDC motor," *IEEE Trans. Magn.*, vol. 56, no. 1, pp. 1–6, Jan. 2020.

[18] A. Apte, V. A. Joshi, H. Mehta, and R. Walambe, "Disturbance-observer-based sensorless control of PMSM using integral state feedback controller," *IEEE Trans. Power Electron.*, vol. 35, no. 6, pp. 6082–6090, Jun. 2020.

[19] H. V. Nguyen, T. Vo-Duy, and M. C. Ta, "Comparative study of disturbance observer-based control and active disturbance rejection control in brushless DC motor drives," in *Proc. IEEE Veh. Power Propulsion Conf.*, 2019, pp. 1–6.

[20] C. Dai, T. Guo, J. Yang, and S. Li, "A disturbance observer-based current-constrained controller for speed regulation of PMSM systems subject to unmatched disturbances," *IEEE Trans. Ind. Electron.*, vol. 68, no. 1, pp. 767–775, Jan. 2021.

[21] L. Li, G. Pei, J. Liu, P. Du, L. Pei, and C. Zhong, "2-DOF robust h_∞ control for permanent magnet synchronous motor with disturbance observer," *IEEE Trans. Power Electron.*, vol. 36, no. 3, pp. 3462–3472, Mar. 2021.

[22] Y. Wang, H. Yu, and L. Y. Liu, "Speed-current single-loop control with overcurrent protection for PMSM based on time-varying nonlinear disturbance observer," *IEEE Trans. Ind. Electron., early access*, 2021. doi: 10.1109/TIE.2021.3051594.

[23] Z. Xu, T. Zhang, Y. Bao, H. Zhang, and C. Gerada, "A nonlinear extended state observer for rotor position and speed estimation for sensorless IPMSM drives," *IEEE Trans. Power Electron.*, vol. 35, no. 1, pp. 733–743, Jan. 2020.

[24] L. Qu, W. Qiao, and L. Qu, "An extended-state-observer-based sliding-mode speed control for permanent-magnet synchronous motors," IEEE J. Emerg. Sel. Topics *Power Electron., early access*, 2020. doi: 10.1109/JESTPE.2020.2990442.

[25] Y. Xu, B. Zheng, G. Wang, H. Yan, and J. Zou, "Current harmonic suppression in dual three-phase permanent magnet synchronous machine with extended state observer," *IEEE Trans. Power Electron.*, vol. 35, no. 11, pp. 12 166–12180, Nov. 2020.

[26] L. Qu, W. Qiao, and L. Qu, "An enhanced linear active disturbance rejection rotor position sensorless control for permanent magnet synchronous motors," *IEEE Trans. Power Electron.*, vol. 35, no. 6, pp. 6175–6184, Nov. 2020.

[27] A. M. Diab, S. Bozhko, M. Galea, and C. Gerada, "Stable and robust design of active disturbance-rejection current controller for permanent magnet machines in transportation systems," *IEEE Trans. Transport. Electrific.*, vol. 6, no. 4, pp. 1421–1433, Dec. 2020.

[28] L. Qu, W. Qiao, and L. Qu, "Active-disturbance-rejection-based sliding-mode current control for permanent-magnet synchronous motors," *IEEE Trans. Power Electron.*, vol. 36, no. 1, pp. 751–760, Jan. 2021.

[29] X. Song, B. Han, and K. Wang, "Sensorless drive of high-speed BLDC motors based on virtual third-harmonic back EMF and high-precision compensation," *IEEE Trans. Power Electron.*, vol. 34, no. 9, pp. 8787–8796, Sep. 2019.

[30] V. Viswanathan and J. Seenithangom, "Commutation torque ripple reduction in the BLDC motor using modified SEPIC and three-level NPC inverter," *IEEE Trans. Power Electron.*, vol. 33, no. 1, pp. 535–546, Jan. 2018.

[31] N. Urasaki, T. Senjyu, and K. Uezato, "Investigation of influences of various losses on electromagnetic torque for surface-mounted permanent magnet synchronous motors," *IEEE Trans. Power Electron.*, vol. 18, no. 1, pp. 131–139, Jan. 2003.
[32] S. Ahmad and A. Ali, "Unified disturbance estimation based control and equivalence with IMC, PID: Case study on a DC-DC boost converter," *IEEE Trans. Ind. Electron., early access*, 2020. doi: 10.1109/TIE.2020.2987269.
[33] Z. Gao, "Scaling and bandwidth-parameterization based controller tuning," in *Proc. Amer. Control Conf.*, vol. 6, Jun. 2003, pp. 4989–4996.

Prashant Kumar (Graduate Student Member, IEEE) received the B.Tech. degree in electrical and electronics engineering from Guru Ramdas Khalsa Institute of Science and Technology, Jabalpur, India, in 2012, and the M.Tech. degree in electrical engineering in 2018 from the Indian Institute of Technology (Indian School of Mines), Dhanbad, India, where he is currently working toward the Ph.D. degree.

He was a Visiting Scholar with the Department of Electrical Engineering and Computer Science, Khalifa University, Abu Dhabi, UAE, in 2020. His research interests include modulation strategies for PMBLDCM motor drives and its control, and sensorless predictive control.

Abdul R. Beig (Senior Member, IEEE) received the B.Eng. degree in electrical and electronics engineering from the National Institute of Technology Karnataka, Surathkal, India, in 1989, and the M.Tech. and Ph.D. degrees in electrical engineering from the Indian Institute of Science, Bengaluru, India, in 1998 and 2004, respectively.

He is currently an Associate Professor with the Advanced Power and Energy Center, Electrical Engineering and Computer Science Department, Khalifa University of Science and Technology, Abu Dhabi, UAE. His current research focuses on autotuning of grid-connected converters, electric vehicle drivetrain, high gain converters, modular multilevel converters, and SiC-based converters.

Dr. Beig is serving as an Associate Editor for the IEEE TRANSACTIONS ON INDUSTRY APPLICATIONS.

Devara Vijaya Bhaskar (Member, IEEE) received the B.Tech. degree in electrical and electronics engineering from Jawaharlal Nehru Technological University Hyderabad (JNTU), Hyderabad, India, in 2006, and the M.Tech. degree in power electronics and drives and the Ph.D. degree in electrical engineering from the National Institute of Technology, Warangal, India, in 2009 and 2017, respectively.

He is currently an Assistant Professor with the Department of Electrical Engineering, Indian Institute of Technology (Indian School of Mines), Dhanbad, Jharkhand, India. His research interests include low cost drive converters for electric vehicle and household appliances, and nonlinear control.

Khaled Al Jaafari (Senior Member, IEEE) received the B.Sc. and M.Sc. degrees in electrical engineering (EE) from the Petroleum Institute, Abu Dhabi, UAE, in 2006 and 2011, respectively, and the Ph.D. degree from the Department of Electrical and Computer Engineering, Texas A&M University, College Station, TX, USA, in 2016.

He is currently an Assistant Professor with the Khalifa University of Science and Technology, Abu Dhabi, UAE. His research interests include machines condition monitoring, power system analysis, power system protection, and power quality studies.

Utkal Ranjan Muduli (Member, IEEE) received the B.Tech. degree in electrical and electronics engineering from Biju Patnaik University of Technology Odisha, Rourkela, India, in 2011, and the M.Tech. degree in electrical engineering from the Indian Institute of Technology Gandhinagar, Ahmedabad, India, in 2014. He is currently working toward the Ph.D. degree with the Indian Institute of Technology Patna, Daulatpur, India.

He was a Visiting Scholar with the Department of Electrical Engineering and Computer Science, Khalifa University, Abu Dhabi, UAE, in 2019. His research interests include modulation strategies for multiphase motor drives, matrix converters and its control, battery power management, and wireless power transfer.

Ranjan Kumar Behera (Senior Member, IEEE) received the B.Eng. degree in electrical engineering from the Regional Engineering College (NIT) Rourkela, Rourkela, India, in 1998, and the M.Tech. and Ph.D. degrees from the Indian Institute of Technology Kanpur, Kanpur, India, in 2003 and 2009, respectively.

He was a Visiting Scholar with the Energy Systems Research Center, Tennessee Technological University, Cookeville, TN, USA, in 2008. He has been a faculty member since 2009 and is currently an Associate Professor with the Department of Electrical Engineering, Indian Institute of Technology Patna, Daulatpur, India. In 2016, he was a Visiting Research Collaborator with the Department of Electrical, Electronic and Computer Engineering, University of Pretoria, Pretoria, South Africa. He is the author of more than 100 scientific papers published in conference proceedings and international journals. His research interests include nonlinear control theory application to power electronic converters, pulsewidth modulation techniques, and multiphase electric drives control.

Dr. Behera has received many national and international awards such as Young Scientists Award in Engineering Sciences, DST, Government of India, in 2001 and Bhaskara Advanced Solar Energy (BASE) Indo-U.S. Science and Technology Forum for Solar Research in the USA in 2014, and was selected as the Featured Engineer of the Globe 2015.